Experimental and Analytical Investigation of a Main Coolant Pump

E. J. Gunter, University of Virginia, Charlottesville, Virginia

J. T. O'Brien and J. T. O'Brien, Jr., O'Brien Group Inc., Paoli, Pennsylvania

This article deals with the dynamic and static analysis of a vertical motor driven main coolant pump using transfer matrix and finite element methods on a microcomputer. This particular class of vertical motor water pump has experienced thermal cracking near the pump bearing bracket support. The object of the study was to obtain a computer model which matched the experimental data and to examine the possibility that static and dynamic loads on the motor-pump system could increase the rate of crack propagation. A critical speed analysis of the motor-pump system with casing effects was performed using the transfer matrix method. These mode shapes matched experimentally determined data. A finite element model was developed using MSC/PAL2 which gave excellent agreement with the transfer matrix analysis. Using the finite element model, the axial and torsional natural frequencies of the pump were also determined. The stresses at the bearing cartridge were analyzed under various combinations of axial, radial and torsional moments. It was concluded that the combined action of torsional and radial loading could enhance the rate of crack propagation observed in this class of pump.

Figure 1 is a schematic diagram of a vertical water pump driven by a variable speed motor. This class of pump, which has been in operation for over ten years, has been experiencing cracks above the hydrostatic pump journal bearing. There is a large thermal gradient at this location which has led to thermal shaft cracking.[1] However, the theory of thermal shaft cracking has not been sufficient to explain the crack propagation at this location.

Vibration instrumentation has been used on several of these pumps to determine if there are any excessive vibration modes in the system.[2] Figure 2 shows the location of various transducers placed within the motor-pump system. Velocity probes were placed on the upper motor casing and displacement probes were placed at the coupling to monitor the shaft motion.

Various spectra were obtained on the pump under different conditions of speed and loading. Figure 3 shows the spectrum for start-up at: (A) 387 RPM low speed; (B) 653 RPM; and at (C) the operating speed range of 1,183 RPM. The motor bearings in this system are plain journal bearings. In Figure 3A, half frequency oil film whirl is shown in the system. Also, a 5 times running speed or 5× vibration is illustrated. As the pump increases in speed and the loading on the impeller increases, Figure 3B shows that the half frequency whirl diminishes but that there is substantial 5× excitation on the pump. As the speed of the rotor increases to 1,183 RPM, it is seen that the 5× excitation reduces by a factor of 3. The high value of the 5× excitation at 653 RPM is indicative of the excitation of a structural resonance frequency in this system. This would place the resonance frequency at 3,165 CPM.

Figure 4 represents the amplitude at the shaft using 5× order tracking. From the shape of the amplitude response and the phase change, it is apparent that there is a significant resonance frequency in the rotor which is being excited by the 5× pulses from the impeller. One of the objectives of this study, therefore, was to model the motor-pump system to determine the nature of the resonance frequency and to see if it contributed to the crack propagation at the pump bearing.

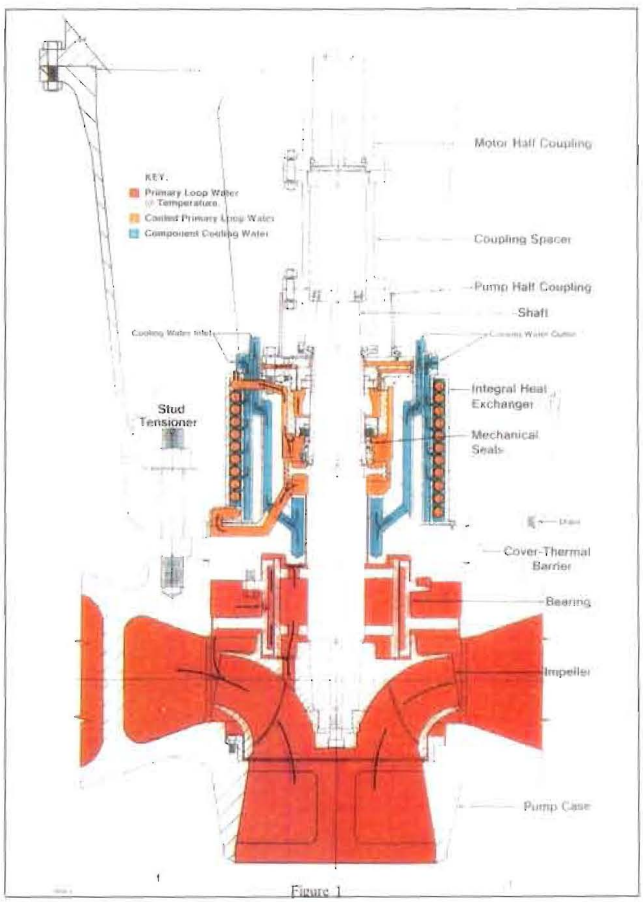

Figure 1. Schematic diagram of a vertical water pump.

Figure 5 shows the synchronous amplitude and phase of the motor up to 1,200 RPM. It is apparent from the synchronous amplitude and response that there is no rotor critical speed in the operating speed range. However, resonance frequencies of the motor casing were observed.

From the displacements measured at various transducer locations, estimates of the pump shaft deflection were made for 1× and 5× excitation.[11] For example, Figure 6 represents the extrapolated pump shaft mode shape at 1,250 RPM based on experimental data. Figure 7 illustrates the 5× pump shaft deflection at 640 RPM determined by a cubic spline fit. Figure 7 shows the estimated motor-pump mode shape based on the available experimental data.

The data obtained on this pump are rather remarkable in that the amplitude and phase for 5× excitation were recorded showing the obvious existence of a higher order resonance frequency in the motor-pump system which appears to be excited by the five blade impeller. It has been conjectured that the thermal cracks may be driven by mechanical loading. It was, therefore, the object of this study to determine if static or dynamic loading could be responsible for accelerating the cracks obtained in the pump shaft due to thermal cycling.

Based on a paper presented at the 16th Annual Meeting of the Vibration Institute, Williamsburg, VA, June 1992.

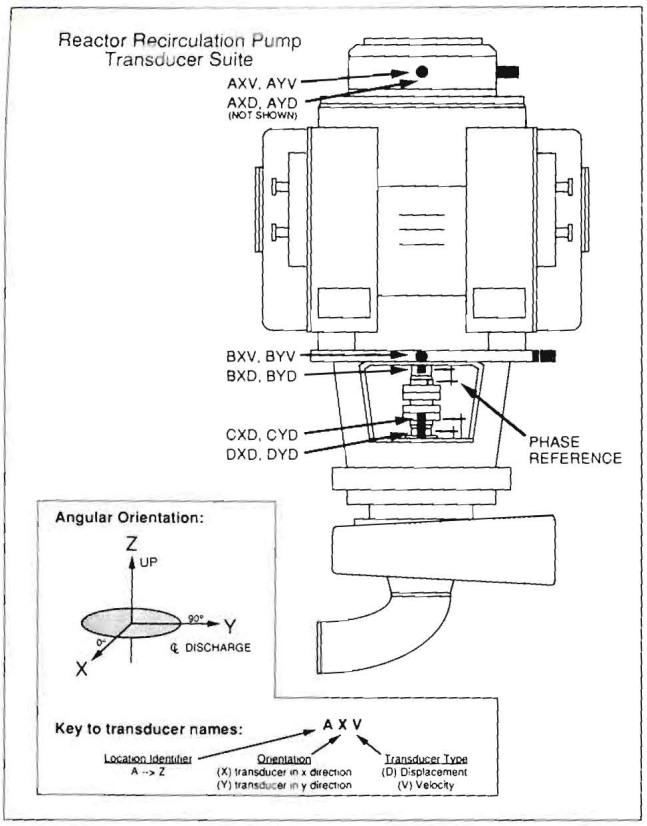

Figure 2. Location of various transducers on motor-pump system.

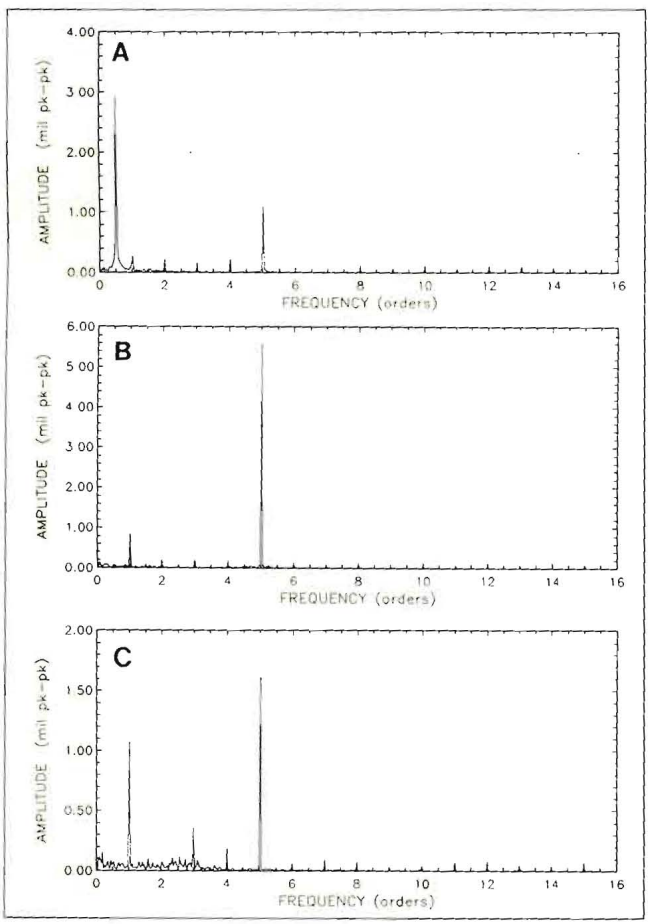

Figure 3. Vibration characteristics of pump seal at various speeds: (A) shaft vibration at 387 RPM showing large half-frequencey whirl component; (B) shaft vibration at 653 RPM showing large 5× component; and (C) shaft vibration at 1183 RPM showing synchronous (1×) and reduced 5× component.

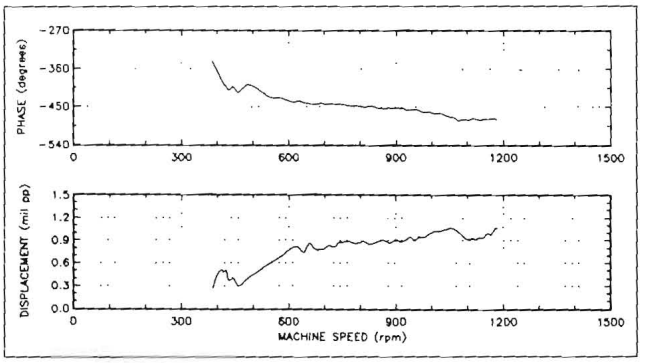

Figure 4. 5× order tracking showing amplitude and phase response at the shaft.

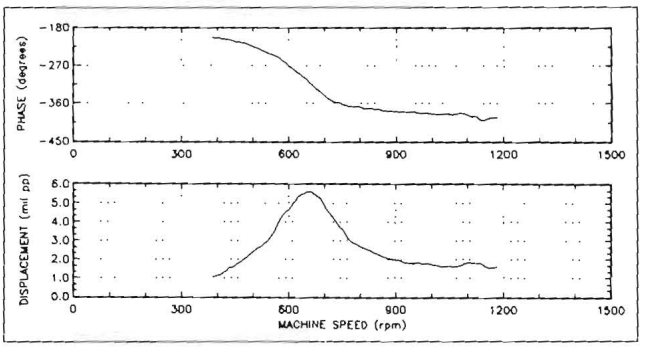

Figure 5. Pump startup synchronous amplitude and phase.

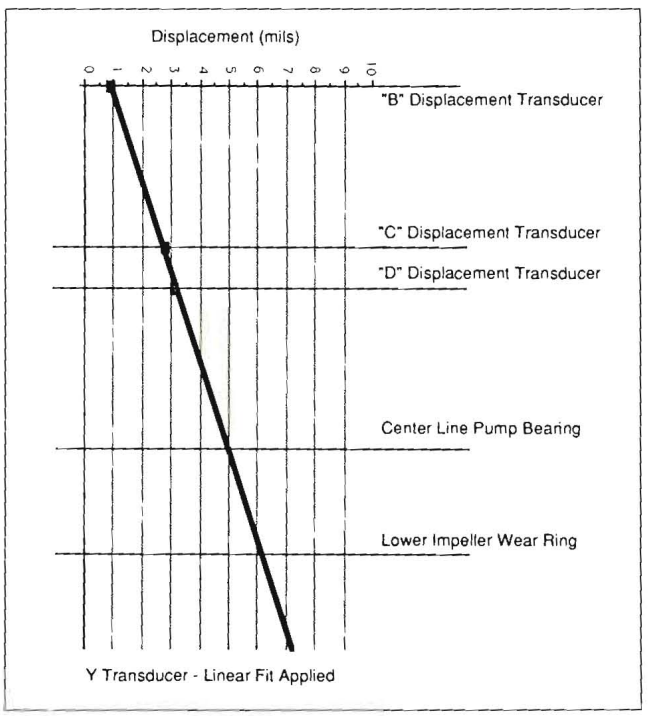

Figure 6. Extrapolated pump shaft mode shape based on experimental data (at 1250 RPM).

Critical Speeds of Motor-Pump System

The first procedure in the dynamic analysis of the motor-pump was to compute the lateral critical speeds. The lateral critical speed analysis computes the undamped natural frequencies of the system. In the original design of this system, the lateral and torsional critical speeds of the combined motor-pump system were not investigated since they were assumed to be above the operating speed range of the system. However, because of the experimental evidence of 5× pump excitation, it was considered necessary to compute both the lateral and the torsional critical speeds to at least 5 times the

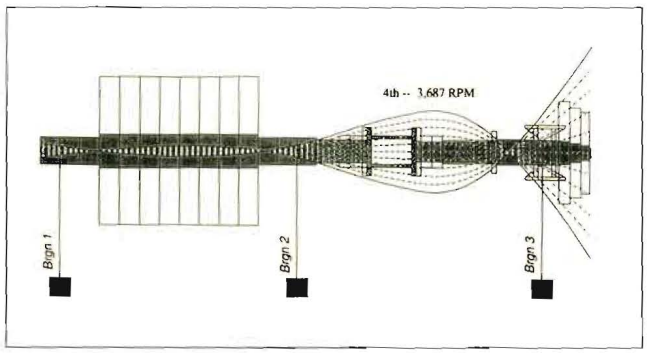

Figure 13. Mode shape of fourth critical speed.

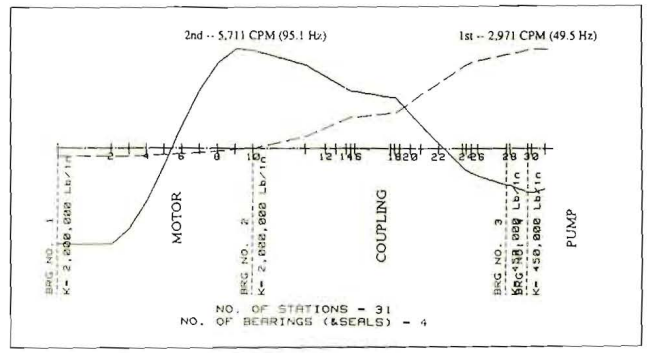

Figure 14. Motor-pump first and second torsional modes at 2,971 CPM and 5,711 CPM.

is obtained in which the rotor and foundation are out of phase.

Figure 12 represents the motor-pump first five modes below 7,000 RPM. The first motor-pump mode is essentially a motor mode at 2,071 RPM. In this mode, the motor and foundation motion are in phase. The introduction of the motor casing masses cause only a slight reduction in the motor first critical speed. The pump has very little influence on this particular mode. This mode is well damped by the fluid film motor bearings and should not be excited either by 1× or 5× pump excitation. The second mode at 2,228 RPM is essentially an overhung cantilever pump mode. Note that the experimentally measured mode as shown in Figure 6 does not appear to correspond to the first pump mode.

Figure 13 represents the system fourth mode at 3,687 RPM. This mode is also in the same frequency range as that observed experimentally at the coupling. In this mode, over 64% of the system kinetic energy is associated with the pump impeller. The pump bearing has approximately 50% of the system strain energy, and the strain energy of the motor support is only 9%. There is 20% kinetic energy associated with the pump casing. However, by including the pump casing in the model, the mode shape has changed considerably from the mode shape of the pump alone. The mode shape now looks very similar to the estimated mode shape shown in Figure 7 based on experimental data. It is impossible to generate a mode shape similar to that shown in Figure 7 unless the pump casing effects are included in the model. This model also indicates the importance of placing accelerometer or velocity pickups on the pump casing in order to monitor the casing motion.

From the study performed on the critical speed analysis of the motor-pump system, it is apparent that casing or foundation mass effects may play an important roll in determining the critical speeds and the mode shapes. Therefore, it is essential to instrument the motor-pump casing as well as the shaft for the determination of the complete system mode shapes. This situation of casing interactions with the rotor modes is well known for large turbine-generators and is normally taken into consideration by the manufacturers. The casing impedance characteristics may be determined experimentally by means of a vibration exciter and an FFT analyzer. Impedance measurements of casings and foundations are now a standard procedure in industry. As a general rule, all rotating elements over 2,000 lb usually have casing or foundation effects associated with them. Therefore, it is concluded that for proper dynamic analysis of a large vertical motor-pump system, casing-foundation effects should also be taken into consideration.

Torsional Critical Speed Analysis. Torsional critical speeds were computed for the combined motor-pump system using a transfer matrix[5] and finite element methods using MSC/PAL2.[13] In the original design and analysis of this system, no torsional critical speeds were computed because it was felt that they would be above the operating speed range. From the experimental data, however, it was seen that there is a substantial 5× excitation due to the interaction of the 5 blade impeller with the discharge volute. Therefore, torsional pulsations can be generated in the pump and it is necessary to examine the torsional critical speeds up through 5× the operating speed range.

The evaluation of the location of the torsional critical speeds is of particular importance, especially with this type of unit. A variable frequency motor is used in which a wide range of operating speeds can be achieved. There are many circumstances when the pump must operate at partial flow with a reduced speed. It is extremely important not to operate near or at the vicinity of a torsional critical speed or to have a multiple of the blade passing frequency correspond to a torsional critical as torsional stresses may be greatly amplified. Figure 14 represents the first two torsional critical speeds of the motor-pump at 2,971 CPM and 5,711 CPM which may be excited at operating speeds of 594 and 1142 RPM.

It is apparent from the torsional analysis that the operating speed range of 1,000 to 1,200 RPM may be undesirable because of the possible excitation of a second torsional critical speed in the operating speed range by the 5× blade passing frequency. The motor has relatively little effect on the first torsional critical speed. However, the motor has a considerable influence on the second critical speed. Using finite element techniques, the motor core may be modeled as a separate body attached to the motor shaft. This produces more realistic torsional models than treating the motor as a single entity.

Natural Frequencies Using Finite Element Methods

In this study, it was determined that the rotor critical speeds, or lateral natural frequencies, may be accurately computed using finite element techniques when the disk gyroscopic effects are minimal. By ignoring the shaft and disk gyroscopic moments, rotor critical speed simulation may be reduced to lateral beam vibrations. The model is reduced to planar motion in the X-Y plane. Gyroscopic moments may be incorporated into the mainframe NASTRAN finite element code by means of skew symmetric damping matrices. This provision, however, has not been implemented yet on any finite element PC versions.

It should be emphasized that one of the major advantages of the finite element technique is that the same model may be used for lateral, torsional and axial modes of motion by changing the constraints of the system. Also, shaft material properties may be easily varied along the rotor by means of the material properties command.

Finite Element Analysis of Motor-Pump System With Foundation Effects. One of the powerful features of the finite element procedure is the ability to put in foundation structures of considerable complexity. This is one of the major drawbacks of the transfer matrix method. In order to represent the effect of the foundation, additional nodes must be included at each bearing location. Lumped masses are placed at the nodes to simulate the motor and pump casing masses. More complex three-dimensional casing models have been investigated.

One must be very careful when developing a finite element model with springs in series. There is no lateral stiffness across the spring interface. Therefore, one must either zero out the displacements in the out-of-plane direction or add a constraining spring. In this model, three extra node points were introduced along the axis in line with the journal bearing

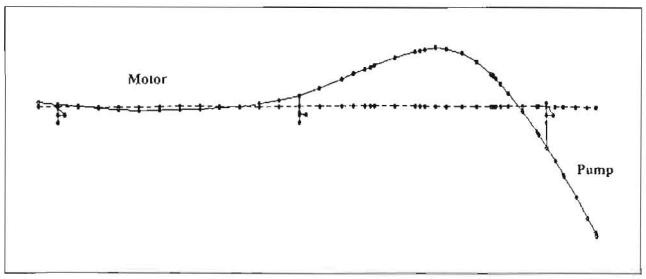

Figure 15. Finite element mode shape of first natural frequency (N_1 = 3,724 RPM) - combined model with foundation.

nodes. Stiff springs of the order of 1.0×10^7 lb/in. were used to constrain the casing masses in the axial direction.

In order to calculate the natural frequencies of the system, there are a number of important constraints that must be applied to the model in order not to obtain a singular stiffness matrix. The first set of constraints corresponds to the ground nodes which are zeroed out. The second set of constraints refers to the assumption of planar modes in which the out-of-plane displacements and rotations are eliminated. A very subtle constraint that must be applied is to zero out all angular rotations at the intersection of the journal bearing at the foundation. Hence, the lumped mass of the casing contains no moments of inertia, and rotational degrees of freedom are not desired. In applying this final constraint, the modes for the combined motor-pump system with foundation effects were successfully calculated.

Table 1 represents the first four motor-pump modes with foundation effects in comparison to the values obtained by the transfer matrix method. The finite element model produced unusually good agreement with the critical speed model as the differences between the two procedures is less than 2%. The mode shapes were also in excellent agreement. Figure 15 represents the motor-pump fourth natural frequency at N = 3,724 RPM with foundation effects.

Axial Natural Frequencies of Motor-Pump System by Finite Element Method. Although the finite element model has been developed primarily for lateral and torsional modal analysis, it is of interest to note that the axial modes of motion may be easily determined by unconstraining the axial displacements. Axial modes are normally not a problem with most turbo-rotors but should be taken into consideration with long multi-span turbine-generators and large vertical motor-pumps. The length and weight of this system is of significant magnitude to warrant investigation of the axial modes.

In order to determine the axial modes of motion, the system is constrained in all of the degrees-of-freedom except the axial coordinates. An additional ground node was placed near the thrust bearing. An axial spring, representing the thrust bearing, was then connected to the thrust bearing. The first four axial modes were calculated for a range of thrust bearing stiffnesses.

Figure 16 represents the motor-pump first axial mode for various values of thrust bearing stiffness. It is seen that, for a thrust bearing stiffness of approximately 1.2×10^6 lb/in., the first axial mode is at the design operating speed. This implies that there may be the existence of an axial or "pogo" mode. The axial or pogo mode may be significant in motor-pump systems with rolling element bearings because of the lack of inherent damping in the system. From this analysis, it is concluded that

Table 1. Comparison of critical speeds using transfer matrix and finite element method for motor-pump system with foundation effects.

Mode	Transfer Matrix (RPM)	Finite Element Method (RPM)	% Error
1	2,071	2,037	1.6
2	2,228	2,248	−0.9
3	3,444	3,426	0.5
4	3,687	3,724	−1.0

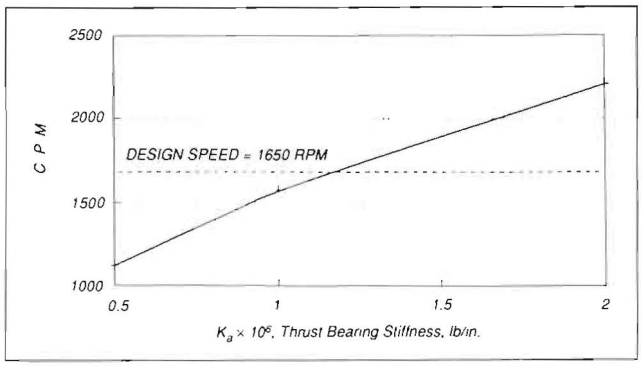

Figure 16. Motor-pump first axial mode for various values of thrust bearing stiffness.

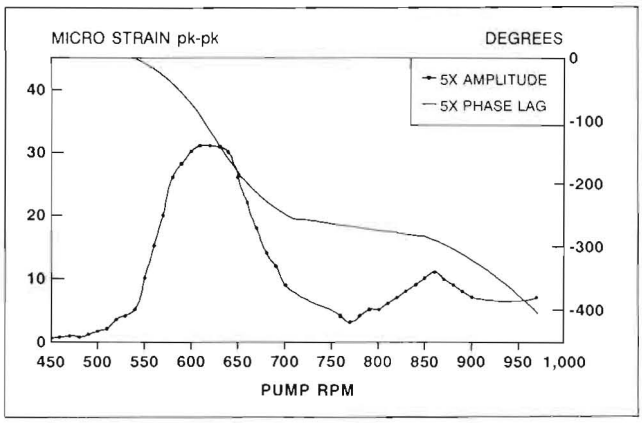

Figure 17. Torsional amplitude and phase lag with 5× tracking vs pump RPM.

instrumentation should be mounted on the coupling to monitor the axial motion of the shaft.

Torsional Natural Frequencies of Motor-Pump System by Finite Element Method. The torsional analysis of a turbo-rotor using finite element techniques requires additional components to be added to the rotor model. In the earlier motor-pump models, the mass command was used to specify lumped masses. The finite element mass command in MSC/PAL2 may also be used to specify the principal moments of inertia of the body. The first principal moment of inertia for the X direction corresponds to the polar moment of inertia for the rotor. The polar moments of inertia were specified for the various components of the motor and pump based on calculated values of I_p from the critical speed program.

The first and second torsional critical speeds were computed to be 44.39 Hz (2664 CPM) and 96.09 Hz (5,765 CPM) respectively. These modes are in error by only 4.2% and 1.4% for the first and second modes computed by the Holzer (transfer matrix) method. The second torsional mode is strongly affected by the diameter assumed at the motor center. If, for example, an effective larger motor shaft diameter is assumed, then the second torsional mode would increase higher than 5,765 CPM. The increase of the second mode to above 5,700 RPM is significant because of the 5× pump excitation throughout the operating speed range. It would be highly undesirable to have any torsional modes between the vicinity of 5,000 and 8,000 CPM because of the possibility of excitation with the variable speed drive system.

In the computation of torsional critical speeds by the transfer matrix method, the motor core is often treated as a single body or lumped inertia attached to the shaft. This assumption is satisfactory for the computation of the motor-pump first torsional critical speed, but is greatly inadequate for the calculation of the higher modes. By using finite element techniques, the motor core may be treated as a separate elastic body connected to the shaft by a distributed rotational stiffness spring. Additional torsional modes may be obtained which are not

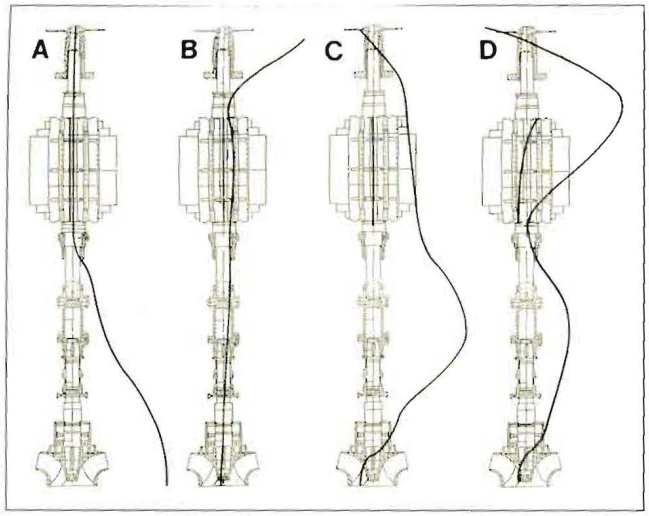

Figure 18(A). Motor-pump first torsional mode by finite element method - 2,640 CPM (44 CPS), $K_t = 10^7$ lb-in., $E_{Motor} = 10^6$ lb/in^2. (B) Motor-pump finite element second torsional mode - 8,040 CPM (134 CPS), $K_t = 10^7$ lb-in., $E_{Motor} = 10^6$ lb/in^2. (C) Motor-pump third torsional mode - 15,180 CPM (253 CPS), $K_t = 10^7$ lb-in., $E_{Motor} = 10^6$ lb/in^2. (D) Motor-pump fourth torsional critical speed - 18,180 CPM (303 CPS), $K_t = 10^7$ lb-in., $E_{Motor} = 10^6$ lb/in^2.

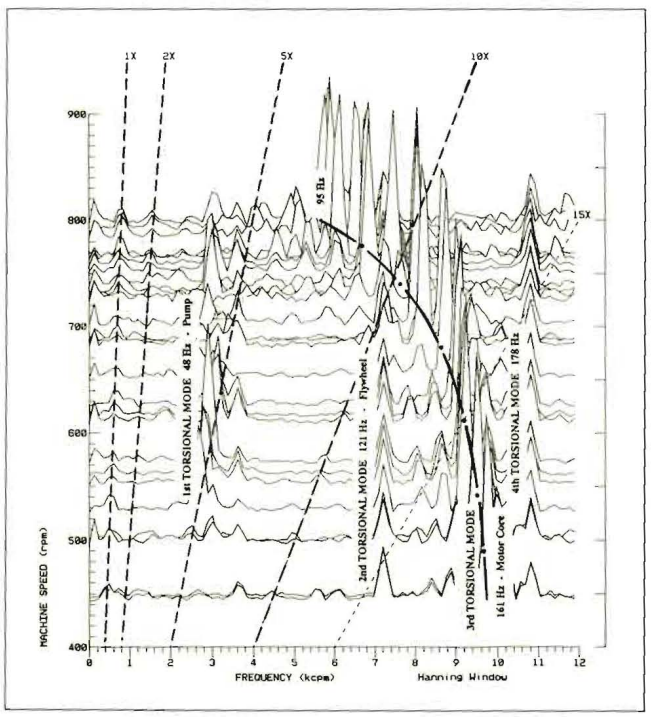

Figure 19. Torsional spectrum vs pump speed under startup conditions.

observed when using the simple transfer matrix method, assuming a lumped mass motor model. The second torsional mode at 5,765 CPM was obtained by assuming a distributed motor core along the shaft. Additional modes are obtained by considering an elastic motor core torsionally coupled to the shaft. Preliminary torsional strain data indicates the presence of higher torsional modes.

Figure 17 represents the torsional microstrain amplitude recorded near the coupling on a vertical nuclear water pump tracking the 5× excitation component generated by the 5 bladed pump impeller. At a rotor speed of approximately 610 RPM, the first torsional critical speed of the pump is clearly evident. Since the 5× component of vibration only is being tracked along with phase, the first natural torsional frequency corresponding to 610 RPM is 3,050 CPM. This corresponds to a first torsional frequency of 50.8 Hz.

Figure 18A represents the first torsional mode shape super-

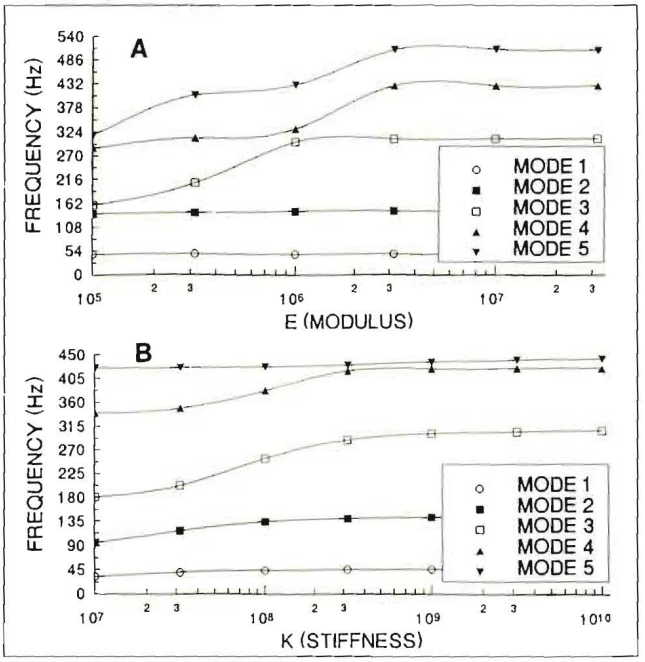

Figure 20. (A) Influence of motor modulus E on pump torsional critical speeds. (B) Influence of motor torsional stiffness K_t on pump torsional critical speeds.

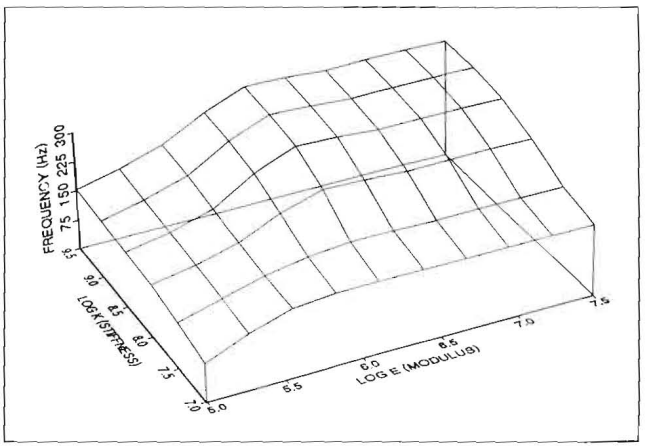

Figure 21. Three-dimensional plot of pump third torsional critical speed as influenced by motor K_t and E_{Motor}.

imposed upon the nuclear water pump. The natural frequency of the computed first torsional mode using finite element methods is 44 CPS. This mode corresponds closely to the first torsional calculated by the Holzer or transfer matrix method. In the finite element motor-pump torsional analysis, the motor was treated as a separate elastic cylinder torsionally connected to the shaft. For the first mode, there is very little torsional activity in the motor. The first mode has a very large angular displacement at the pump with a small counteracting angular displacement at the motor. This is due to the large value of the polar moment of inertia of the motor in comparison to the pump. The calculation of the higher torsional modes is of greater complexity due to the torsional interaction of the motor core which is connected to the shaft by a spider cage.

Figure 19 represents the startup torsional data obtained on a recirculation pump. A spectrum of the torsional vibrational data was obtained for various values of rotor speed from 450 RPM to 800 RPM. The dotted lines on the plot correspond to 1, 2, 5 and 10 times running speed. On this plot are labeled what appear to be four distinct torsional resonant frequencies.

The first observed torsional resonant frequency appears to be 48 Hz. This is the pump mode which is excited by 5× running frequency and is shown in Figures 14 and 18A. The second torsional mode shown is at 121 Hz and is not of large

amplitude. This mode is believed to be the local excitation of the flywheel at the top of the motor. Figure 18B represents the second torsional mode with the flywheel included. This is a local mode that is only involved with the upper shaft and flywheel above the motor. This mode is not shown in the transfer matrix analysis of Figure 14 since the flywheel was not included in the model.

The torsional mode of considerable interest and controversy is the third mode which appears to decrease in frequency with increasing rotor speed. It is postulated that the third mode occurs at 161 Hz at 450 RPM and reduces in frequency to 95 Hz at 800 RPM. There appears to be a large amount of torsional energy in this mode and it may be caused by the interaction of the motor core with the shaft. The 95 Hz frequency corresponds to the calculation of the second mode using the transfer matrix method in which the motor mass polar moment of inertia is distributed along the shaft.

In order to better understand the nature of the interaction of the motor core with the shaft, a detailed torsional analysis was performed using the finite element technique in which the elasticity of the motor core was varied in addition to the torsional stiffness of the connection of the motor core to the shaft. Figures 20A and 20B represent, respectively, the influence of the modulus E (or G) of the motor on the first four torsional critical speeds. Figure 20B represents the influence of torsional stiffness connecting the motor core to the shaft. From Figures 20A and 20B, it is seen that the spider cage torsional stiffness or the motor E value has very little influence on the first two torsional critical speeds. However, the third mode is greatly influenced by the combination of the motor E and the torsional stiffness K_t.

Figure 21 represents a three-dimensional plot of the third torsional critical speed as a 2-dimensional function of the motor shaft torsional stiffness K_t and the motor modulus E. This shows that the third torsional critical speed can vary from as high as 300 Hz to as low as 75 Hz, depending upon the motor E and K_t values.

It is speculated that if the high activity seen in the spectrum plot is indeed a third torsional critical speed, then it may reduce with speed due to the heating up of the motor core. As the motor core becomes hotter, the value of E will reduce as the windings heat up. From Figure 19, it is also of interest to note that at approximately 750 RPM, the 10× excitation line intersects with both the second and the third modes. Considerable activity is seen at this speed.

Figure 18C represents a typical third torsional mode predicted to be 253 CPS with $K_t = 10^7$ lb-in. and $E = 10^6$ lb/in^2. Note that the motor core shows little activity for this mode. This particular mode does not correspond to the mode shape as produced by the transfer matrix method with the distributed motor inertia along the shaft. To produce the second mode shape generated by the Holzer method, as shown in Figure 14, the E value must be reduced to an extremely low value as shown in Figure 21. If the entire motor is treated as a lumped inertia, then the third mode vanishes.

Figure 18D represents the fourth mode at 303 CPS assuming a torsional stiffness of $K_t = 10^7$ in.-lb and $E = 10^6$ lb/in^2. As the E and K_t values are reduced, the activity between the motor and shaft increases.

It is apparent from the torsional critical speed analysis that the standard transfer matrix method of torsional analysis may not be adequate for the analysis of motor-pump systems with large motor cores. The motor core must be treated as a separate cylinder torsionally connected to the shaft. This is extremely difficult to do using the Holzer transfer matrix method as singular branch solutions are often generated by the second span. This numerical problem is not encountered by the finite element method. It is also apparent that the 5 and 10 times excitation forces generated by the pump impeller may excite torsional critical speeds in the system. Further study needs to be conducted on this class of pump to verify the nature of the apparent higher order torsional critical speeds observed in the torsional vibration spectrum.

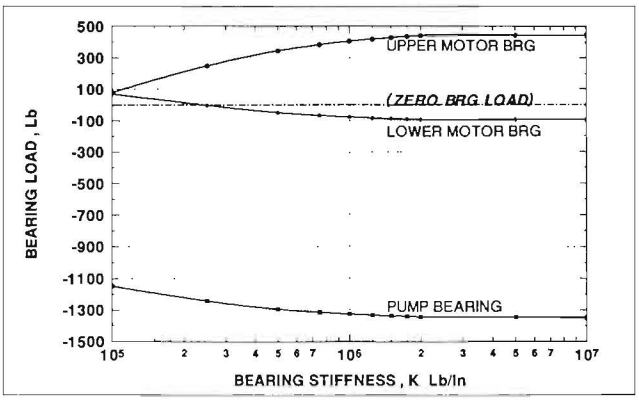

Figure 22. Nuclear water pump static bearing reaction forces for various values of bearing stiffness for 1,000 lb radial pump loading.

Bearing Reaction Loads

Finite element methods may be used to determine the bearing static reactions due to an applied load acting at the pump impeller. For the vertical nuclear water pump, the bearing reaction loads are generated by the dynamic loads of rotor unbalance and static and dynamic loads exerted by the pump impeller. It has been estimated that the pump radial forces may vary from 500 to 1,000 lb radial loading depending upon the specific speed of the pump. The computation of the bearing reactions is similar to the problem of computing the bearing reaction loads of a beam on multiple flexible supports. Since three bearings are involved, the motor-pump is a statically indeterminant structure. The elasticity of the rotor and the bearing stiffness values must both be taken into consideration.

The bearing reaction forces were computed assuming a range of nominal bearing stiffness values from 0.25×10^6 to 2.0×10^6 lb/in. A radial load of 1,000 lb was assumed acting at the impeller. Figure 22 represents the nuclear water pump static bearing reaction forces for various values of bearing stiffnesses with the 1,000 lb radial loading acting at the impeller. Since the impeller is overhung, the largest reaction force occurs at the pump hydrostatic water bearing. It is of interest to note that for bearing stiffness values from 0.75×10^6 to 2.0×10^6 lb/in., there is little variation in the bearing reaction forces.

Of considerable concern is the low value of radial bearing reaction force on the upper motor bearing. For the assumed radial loading of 1,000 lb acting on the impeller, the upper bearing only has a reaction loading of approximately 100 lb. The current bearing design used in the upper and lower motor bearings is an axial groove fluid film bearing. Plain and axial groove bearings in vertical rotors have a tendency to become unstable under light load conditions.

The experimental data shown in Figure 3A shows that at 387 RPM there is a large half-frequency whirl component in the pump. It is believed that this whirl component is due to the light load on the motor bearings. Whenever vertical rotors are operated in plain or axial groove bearings under light load, half-frequency oil whirl may develop. Figure 3C shows that the half-frequency whirl vanishes at the higher speeds due to the increase in loading on the upper motor bearing. This data, however, was taken at partial pump load capacity in which high pump radial loads are developed. There is concern that when the pump is operated at full speed and design conditions, the reduced radial loading at the impeller will not be sufficient to load the upper motor bearing. As rotor speed increases, the pump becomes more susceptible to half-frequency oil film whirl. To correct this problem and to ensure that half-frequency whirl does not occur, the upper motor bearing should be replaced by a tilting pad bearing. Replacing both upper and lower motor bearings would ensure that half-frequency oil whirl does not occur at full speed design conditions in which the radial pump loading is at a minimum.

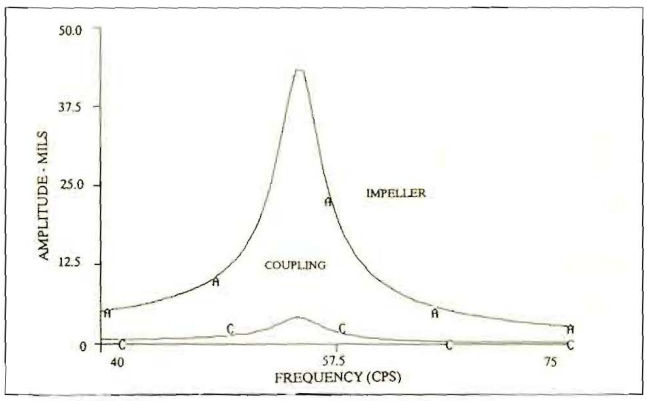

Figure 23. Lateral response of impeller and coupling with a simulated 5× excitation of 1,000 lb from 40 to 75 Hz.

Dynamic Simulation of Motor-Pump System

One of the significant vibrational characteristics of the vertical motor-pump system was the discovery that the pumps have a 5× excitation which could excite a system resonance frequency at approximately 3,400 CPM with the pump running at 680 RPM. By means of a tracking filter, the amplitude and phase for several positions along the coupling were recorded as shown in Figure 4. Since the impeller is a 5 blade design, a 5 times running frequency excitation is generated in the system. One of the system unknowns is the magnitude of the 5× forcing function that the pump may generate.

One of the capabilities of the MSC/PAL2 finite element program is the ability to determine the forced response of the system with a dynamic excitation. A harmonic exciting force of 1,000 lb acting at the impeller was applied for a frequency range of 40 to 75 Hz. One of the other essential elements, in order to correctly calculate the dynamic response, is the amount of damping acting at the various bearings. In the finite element program, only one of the principal components of damping may be applied (no bearing cross coupling effects). For the case of the upper fluid film motor bearing, eight bearing stiffness and damping coefficients were generated. These coefficients can further be reduced to 4 synchronous stiffness and damping coefficients corresponding to the X-Y planes. A nominal value of bearing stiffness of 2.0×10^6 lb/in. and damping of 8.0×10^3 lb-sec/in. for the motor bearings was assumed. It was found that there could be a considerable variation in the assumed motor bearing characteristics without appreciably affecting the results.

The characteristics of the hydrostatic bearing were furnished by the pump manufacturer and the computed stiffness varied between 0.7×10^6 and 0.9×10^6 lb/in. The hydrostatic pump damping for the bearing was determined to be less than 30 lb-sec/in. This unusually low damping value for the hydrostatic bearing is similar to what would be encountered with a rolling element bearing. The total effective damping at the impeller-seal location was determined to be considerably higher than the damping obtained from the hydrostatic bearing.

One of the significant experimental plots is the phase associated with the 5× excitation. The rate of change of the phase curve is directly related to the amount of damping in the system. In particular for this mode, the amount of damping at the bearing-impeller region directly affects the slope of the phase curve. A wide range of response curves was generated for various damping values. A value of damping of 200 lb-sec/in. produced a response phase curve similar to the phase angle observed in the experimental data.

Figure 23 represents the harmonic response of the impeller simulating 5× excitation assuming a dynamic load of 1,000 lb. Curve A represents the end of the impeller and Curve C represents the coupling location monitored. The impeller shows an amplitude of over 40 mils. Rubbing of the outer impeller wear ring seal has been experienced and seal clearances there have been opened up to over 100 mils. The coupling amplitude is approximately 4 mils radial or 8 mils peak-to-peak. Since the observed amplitude at the coupling may vary between 3.5 to 5 mils peak-to-peak, it is estimated that the dynamic loading on the shaft caused by the 5× excitation is of the order of 500 to 800 lb. This value of loading by itself is not sufficient to account for shaft cracking. There is very little amplitude observed at the motor bearings which is consistent with the undamped mode shape for the frequency of 3,687 RPM as shown in Figure 23.

The generated response of amplitude and phase for the motor-pump represents the system transfer function. It is seen that the impeller and coupling are 180° out of phase. This phase relationship is the same as that observed in the critical speed mode shape data. It is of interest to compare the relative magnitudes of the impeller and coupling responses. The ratio of impeller to coupling response is approximately 10 to 1. Therefore, if the experimental amplitude at the coupling is determined to be between 4 to 5 mils, then the impeller motion may be assumed to be 10 times larger, between 40 to 50 mils.

The complete finite element motor-pump transfer function analysis on a 386 class computer operating at 25 MHz required only 5 minutes to perform. One powerful advantage of working with finite elements on a microcomputer is that the binary files may be stored after the analysis is completed. This allows one to rapidly review and replot the computed data without requiring a rerun.

Shaft Stresses Due to Static and Dynamic Loading

The vertical recirculation pump has various types of static and dynamic loads acting upon it. On the motor, there is the magnetic pull of the field and the rotor unbalance. These forces have relatively little effect on the impeller. On the rotor, there is the gravitational weight of the system acting downward. The impeller has a net thrust upward due to the hydraulic axial load. This load may be as high as 20,000 lb. There are several types of forces that may act on the impeller. The first type is rotor unbalance due to mechanical unbalance in the wheel. A large hydraulic synchronous loading may also be generated in the impeller by a nonuniformly filled impeller passage. The second type of loading is the nonsynchronous 5× excitation due to the pump blade passing frequency. A more serious type of load, associated with single discharge volutes, is the hydraulic radial loading that may exist when it is operated off of BEP (best efficiency point). This may generate a large radial loading. The presence of a radial load vector acting on the impeller will lead to alternating stresses in the shaft. Radial loads may develop in double as well as single discharge volutes but of lower magnitude. This pump is a double volute design but the response is similar to a single volute since it has a high 5× excitation but only a low 10× excitation. One would expect with a 5 bladed impeller and double volute design to encounter a strong 10× excitation which was not the case.

Although the radial load effect is well known, it is difficult to quantify with a new pump design. The radial load factor must be determined experimentally. There have been a number of instances in the petrochemical industry where single discharge volutes have led to shaft failure because of the excessive loading developed when operating away from BEP.

Another type of mechanical shaft loading that should be considered for vertical motor pumps is the steady state and dynamic torques that may exist in the system. Since the motor is rated at over 7,000 HP, this creates a steady state torque of 276,000 in.-lb acting at the impeller. Of concern also is the possibility of the 5× excitation causing a dynamic fluctuating torque which could excite the motor-pump second torsional resonance speed. Even a small value of fluctuating torque near the resonance frequency could be greatly magnified. Therefore, in addition to radial static and dynamic loading, static and dynamic torsional effects should also be considered acting on the motor-pump system. The magnitude of the dynamic torque is extremely difficult to estimate and requires experimental measurements on the shaft.

Shaft Stresses Due to Steady-State Loads. The shaft stresses were calculated with various combinations of steady state radial and axial loading and torsional moments. One of the advantages of the finite element method is that the same model may be used to calculate static deflections and stresses that are used in the critical speed and dynamics model. The stresses on the shaft were computed first with the individual load components and then the total stress distribution was computed adding the various combinations of loading on the impeller. The first loading distribution that was considered was that of axial loading on the shaft. It was seen that even large axial loads of 20,000 lb at most cause only 700 psi stress in the shaft. At the crack location, there is a stress of approximately 600 psi only. Therefore, the steady-state stress caused by axial loading is minimal.

The Von Mises shaft stresses corresponding to arbitrarily high radial loads of 15,000 and 30,000 lb were computed. For this pump, the bearing cartridge was assumed to contribute to the load path. This causes an abrupt change in stress at node 35. The radial loading then could generate a stress of 5,000 psi at the crack location depending upon the assumed value of radial loading. It is of interest to note that a much higher stress occurs at node 27 which is just beyond the coupling. However, cracking is not encountered at this location since this region is operating in air instead of water. Hence, the endurance life of the material should be significantly higher at the coupling area than adjacent to the bearing cartridge.

Shaft Stresses with Dynamic Axial Loading. The first axial or pogo mode was determined to be at or near the design operating speed and the stresses generated due to an oscillating axial loading were computed. For the case of a rolling element thrust bearing with no damping in the axial direction, the response at resonance would be excessive.

The action of the fluid film thrust bearing provides a considerable amount of damping in the axial direction. The axial response was computed with the incorporation of damping of 2,000 lb-sec/in. which is representative of the damping magnitude encountered with this class of thrust bearing. The sinusoidal axial mode will be approximately 3.5 mils per 1,000 lb of axial excitation force. When damping is included into the calculation of the dynamic axial response, this value is reduced by a factor of 10. Therefore, dynamic axial stresses may be relatively insignificant in comparison to the radial and torsional stresses. However, it is important to note that some failures of motor-pump systems of this size have been encountered when using rolling element thrust bearings rather than tilting pad Kingsbury thrust bearings. The lack of damping of the rolling element bearing may cause premature failure in the presence of an axial or a pogo mode at running speed.

Shaft Stresses with Torsional Moment. With synchronous and variable speed drive motor systems, there is always a concern of instantaneous dynamic torques being applied to the system. For example, with a synchronous motor under 10% voltage reduction, a pulsating torque of 10 times steady state torque can sometimes be achieved. This can cause catastrophic effects on gear box driven machinery. Since the pump produces a 5× excitation, there will be some dynamic torque existing in the system and it may have a considerable effect on the stresses.

Another source of dynamic torsional excitation on the pump could be the excitation of the motor pump second torsional critical speed under variable speed operating conditions. A pulsating torque value of approximately 10% of the steady state torque, 30,000 in.-lb was applied to the rotor system. The torsional response of the shaft over a frequency range of 60 Hz to 130 Hz was investigated. This would correspond to pump operating speeds of 720 to 1560 RPM assuming a 5× torsional excitation.

Figure 24 represents the torsional response near the crack due to a sinusoidal oscillation of 30,000 in.-lb. At the frequency of approximately 96 Hz (or a pump speed of 1,152 RPM), it is seen that a sharp torsional resonance is encountered. This

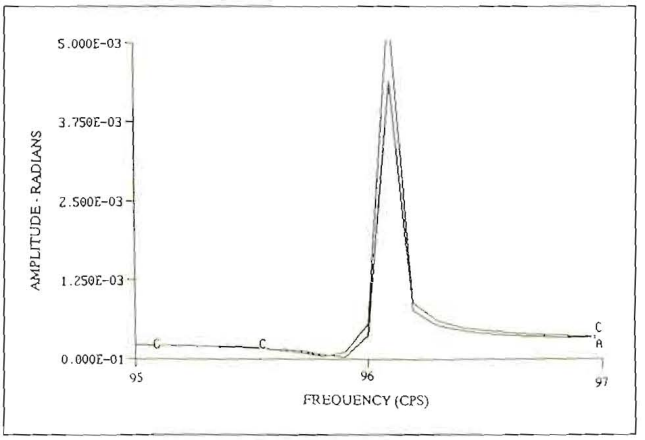

Figure 24. Torsional response of motor-pump system from 95 to 97 Hz.

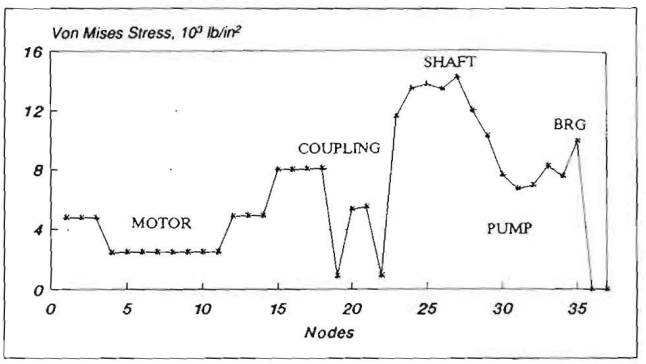

Figure 25. Von Mises stress distribution for combined loading.

implies that, with a variable speed motor, it is possible to transverse this region causing excessive torsional stresses. The shear stress at node 35 is approximately 14,000 psi at the second torsional resonance, with an assumed oscillating torque of 30,000 in.-lb.

There may exist a torsional stress concentration of over 4 at the abrupt change in cross section. Therefore, the total transient torsional stress encountered at node 35 may be well over 50,000 psi. This would be a more than sufficient stress level to cause propagation of the thermal cracks.

Combined Loading. A Von Mises stress distribution was produced with a combined loading of axial, radial and steady state torque as shown in Figure 25. This shows that there is a dramatic increase in the stress at node 35 which corresponds to the crack vicinity. The combined stress is of the order of 10,000 psi. If there are additional dynamic torsional moments applied to the shaft, this stress may increase significantly. It is therefore apparent that the mechanical loading in the vicinity of the thermally induced cracks may aggravate the situation over a long period of time. With the influence of stress concentration factors due to abrupt shaft sectional change, notch and surface grooving in the seal vicinity, these act as stress concentration factors which enhance the effect of the stress distribution. It is shown that the endurance life of steel operating in water is reduced from similar conditions when operating in air.[6] There-

Table 2. Comparison of stresses at cracked region due to various types of static and dynamic loads.

Load	Value	Stress at Cracked Region (psi)	Type of Stress
5× Radial	1,000 lb	300-500	Alternating Mises
Axial	20,000 lb	580	Von Mises
Dynamic Axial	20,000 lb	600	Alternating Mises
Radial	10,000 lb	1,700	Alternating Mises
Steady State Torque	276,000 lb-in	8,500	Von Mises
Dynamic Torsional	30,000 lb-in	27,000	Alternating Mises

fore, even relatively moderate stresses of the magnitude shown here may be of sufficient magnitude to cause the long term failure as experienced in this class of pump.

Discussion and Conclusions

It was the object of this investigation to see if there is a possibility that mechanical loading of various types could be responsible for crack propagation as observed in this class of variable speed motor-pumps. There indeed appears to be a strong possibility that combinations of unidirectional radial and static and dynamic torsional loading of the impeller may substantially contribute to the crack growth initiated by thermal gradients at the seal area near the bearing.

Table 2 shows a summary of the stresses near the pump crack region generated by the various types of loads assumed acting on the impeller. The first loading shown is the dynamic 5× excitation of 1,000 lb. The actual 5× excitation forcing function is estimated to be below this value. The alternating Von Mises stresses are between 300 to 500 psi depending upon the operating speed. The 5× excitation should not be of serious concern.

The next level of stresses shown are the values of stress caused by static and dynamic axial excitation. Although the shaft may be operating on an axial resonance mode, the damping of the thrust bearing should control the motion and axial stresses, for even large axial dynamic loads. This would not be the case if a rolling element thrust bearing were employed on the motor.

The third class of loading investigated are the effects of radial loading. The radial loading acting on the shaft is unidirectional and hence the shaft may act as a fatigue testing machine. The assumed value of 30,000 lb radial loading produces an alternating Von Mises stress of 5,200 psi near the crack area. This value of loading is substantially higher than what was estimated by the pump manufacturer. Further strain gauge testing is required to verify the magnitude of the radial load when operating off of BEP. Such a large value of radial loading should not be encountered with a normal double volute pump design.

The fourth class of loading shown in Table 2 are the stresses due to steady state and dynamic 5× excitation torque. Due to the possible existence of a second torsional critical speed near 5× running speed, small dynamic torques could cause large stresses when the rotor speed corresponds to this speed range. The shear stress concentration factor of over 4 at the pump-bearing sectional change would greatly exacerbate the situation.

In the design of the bearing cartridge for this pump, there is an abrupt change in cross section and there are several factors which are stress raisers acting in the system. These stress factors can magnify the stresses at this location. It is also apparent that the endurance limit of the material operating in water is considerably reduced over the endurance life of the material when operating in air. Although there are higher stress areas in the shaft such as near the coupling location, the combination of stress concentration factors and reduced endurance life of material near the bearing cartridge may be responsible for crack growth.

One of the important conclusions of this study was that there may be higher torsional critical speeds in the system which could be excited by the impeller 5× excitation. It was found that steady state and dynamic torques on the pump may have a significant effect on the overall stress. Because of the significance of the possible existence of higher order torsional critical speeds, instrumentation should be placed on one of these pumps to examine the principal and shear stresses under various operating conditions.

It is concluded that the cracking experienced with this class of pump may not be simply attributed to thermal effects alone, and that the combined static and dynamic stresses encountered during variable speed operations may indeed contribute to crack propagation.

References

1. Beeston, J. M. and Brinkman, C. R., "Axial Fatigue of Irradiated Stainless Steels Tested at Elevated Temperatures," Irradiation Effects on Structured Alloys for Nuclear Reactor Applications, ASTM STP 484, 1970.
2. Begian, D. M. and O'Brien, Jr., J. T., "Lateral Vibration Analysis for Startup Testing of Pumps," *Sound and Vibration*, February 1990.
3. Bently, D. E., "Vibration Monitoring Techniques and Shaft Crack Detection of Reactor Coolant Pumps and Recirculation Pumps," Reactor Coolant Pump and Recirculation Pump Monitoring Workshop, 1988.
4. Brinkman, C. R., et. al., "Influence of Irradiation on the Creep/Fatigue Behavior of Several Austenitic Stainless Steels and Incoloy 800 to 700°C," Effect of Radiation on Substructure and Mechanical Properties of Metals and Alloys, ASTM STP 529, 1973.
5. Colen, R. B. and Gunter, E. J., "Undamped Torsional Critical Speed Analysis of Rotor Systems – A manual for Use with Computer Program CRITSPD," Report No. UVA/643078/MAE81/105, June 1981.
6. Forrest, P. G., *Fatigue of Metals*, Pergamon Press, London, 1962.
7. Gunter, E. J. and Gaston, C. G., *CRITSPD-PC User's Manual*, Rodyn Vibration, Inc., Charlottesville, VA, August, 1987.
8. Huber, K. A., "Considerations for Primary Reactor Pump Monitoring Systems," EPRI Workshop, 1988.
9. Jackson, Charles and Ingram, James H., "Centrifugal Pump Mechanical Performance, Instrumentation, and Diagnostics," *Pump Handbook*, McGraw-Hill, 1986.
10. Kazao, Y. and Gunter, E. J., "Dynamics of Multi-Spool Gas Turbines Using the Matrix Transfer Method-Theory," Proceedings of International Conference on Mechanical Dynamics, Press of Northeast University of Technology, Shenyang, Liaoning, China, August 1987.
11. Kowal, M. G. and O'Brien, J. T., "Monitoring for Shaft Cracks on Reactor Recirculation Pumps," *Sound and Vibration*, May 1989.
12. Maleev, V. L. and Hartman, J. B., *Machine Design*, International Textbook Company, 1954.
13. MSC/PAL2 Reference Manual (Ver. 3.0), The MacNeal-Schwendler Corporation, Los Angeles, CA, November, 1987.
14. Potts, Frank J. and Oler, Walter J., *Finite Element Applications With Microcomputers*, Prentice Hall, 1989.
15. Ruhl, R. L. "Dynamics of Distributed Parameter Rotor Systems: Transfer Matrix and Finite Element Techniques," Ph.D. Thesis, Cornell University, Mechanical Engineering, 1970.
16. Zienkiewicz, O. C., *The Finite Element Method*, McGraw-Hill, 1977.